Studies of Retrogression and Reaging Behavior in a 1441 Al-Li-Cu-Mg-Zr Alloy

K.S. GHOSH, K. DAS, and U.K. CHATTERJEE

A 1441 Al-Li-Cu-Mg-Zr alloy in the peak-aged T8 temper was subjected to retrogression treatment and immediately reaged to various tempers. Transmission electron microscopy (TEM), X-ray diffraction (XRD), differential scanning calorimetry (DSC), hardness measurements, tensile testing, scanning electron microscopy (SEM) fractography, and electrochemical polarization studies have been made to characterize the retrogression and the retrogression and reaging (RRA) behavior of the alloy. Retrogression of the T8 temper causes dissolution of δ' (Al_3Li) precipitates into solid solution, resulting in a decrease of hardness and tensile strength and an increase of ductility. Reaging the retrogressed state causes restoration of strength and ductility properties because of the reprecipitation of the δ' phase in the matrix, confirmed by TEM, XRD, and DSC studies and image analysis. The SEM fractographs revealed predominantly intergranular fracture in all the tempers due to strain localization at the grain boundaries. The gross aging time of the RRA tempers approaches that of the over-aged T7 temper, which would contribute to an improvement of the stress-corrosion cracking (SCC) resistance while maintaining the T8 temper mechanical properties.

I. INTRODUCTION

ALUMINUM-LITHIUM alloys are potential materials for the aerospace industry because of their attractive combination of lighter weight and higher stiffness compared to the most widely used conventional 2*xxx*- and 7*xxx*-series aluminum alloys.[1,2,3] The disadvantages of the Al-Li alloys are poor fracture toughness, low ductility, and marked anisotropy of uncrystallized products.[1,2] The low ductility and toughness of the Al-Li alloys are due to many concurrent and mutually competitive factors; mainly, the inhomogeneous nature of slip resulting from coherent matrix strengthening of ordered spherical δ' precipitates and from the coarse equilibrium δ precipitates at the grain boundaries. However, the presence of Zr, Mg, and Cu in commercial Al-Li-Cu-Mg-Zr alloys causes precipitation of β' (Al_3Zr) dispersoids and semicoherent/incoherent T_1 (Al_2CuLi), S, and S′(Al_2CuMg) phases, which results in better slip homogenization and improvement of the ductility and fracture toughness[4,5,6] of the alloys. Al-Li alloys are also susceptible to stress-corrosion cracking (SCC) in their maximum-strength peak-aged, T6, or T8 tempers. Over-aged T7 temper results in an acceptable SCC resistance, but, because of its lower strength,[7,8,9] components need to be overdesigned.

A heat-treatment process known as retrogression and reaging (RRA), designated as the T77 temper, was developed by Cina *et al.*,[10] and it was reported that the RRA treatment improved the SCC resistance of the aluminum alloys.[11] The principal benefits of the RRA-treated alloys are increased reliability, reduced maintenance costs, and avoidance of weight penalties by the use of the standard overaged T7 temper. Studies on RRA treatment applied to a 7*xxx* series alloy have been reported for optimizing the heat-treatment conditions[12] and for its influence on microstructural changes and precipitation behavior,[13,14,15] on dislocation densities,[16,17] on physical and strength properties,[18,19] and, finally, on the SCC behavior.[15,16,18,20–23] A similar type of work has also been initiated in Al-Li alloys,[24–27] and the results show that RRA treatments increase SCC and exfoliation corrosion resistance. While extensive work has been carried out on characterizing the RRA behavior of 7*xxx*-series alloys, little work is reported on characterizing the RRA behavior of Al-Li-Cu-Mg-Zr alloys. In the present work, the RRA behavior of a 1441 (Russian-grade) Al-Li-Cu-Mg-Zr alloy has been studied by various techniques such as hardness measurements, tensile testing, scanning electron microscope (SEM) fractography, transmission electron microscopy (TEM), X-ray diffraction (XRD), differential scanning calorimetry (DSC), and electrochemical polarization.

II. EXPERIMENTAL PROCEDURES

A. *Materials*

The 1441 Al-Li-Cu-Mg-Zr alloy was obtained from the Defence Metallurgical Research Laboratory (Hyderabad, India), in sheet form, having a thickness of 2.0 mm. The alloy sheet was solutionized at 530 °C to 535 °C, water quenched, stretched 1.5 to 2.5 pct, artificially aged for 4 hours at 150 °C and 24 hours at 170 °C correspond to peak-aged T8 temper. The as-received alloy sheet was aged at 170 °C for 120 hours to obtain the overaged T7 temper. The chemical composition (wt pct) of the alloy is given in Table I. Figure 1, the triplanar optical micrographs of the as-received alloy, shows the grains are more or less equiaxed in all the three longitudinal (L), long transverse (LT), and short transverse (ST) directions. The average grain size of the 1441 alloy has been found to be on the order of 15 to 20 μm.

K.S. GHOSH, Assistant Professor, is in the Department of Metallurgical and Materials Engineering, National Institute of Technology, Warangal - 506 004, India. Contact e-mail: ghosh@nitw.ernet.in. K. DAS, Associate Professor, and U.K. CHATTERJEE, Professor, are in the Department of Metallurgical and Materials Engineering, Indian Institute of Technology, Kharagpur - 721 302, India.

Manuscript submitted October 6, 2004.

Table I. Chemical Composition (Weight Percent) of the 1441 Alloy

Alloy	Li	Cu	Mg	Zr	Fe	Si	Al
1441	1.90	2.0	0.90	0.09	0.11	0.05	balance

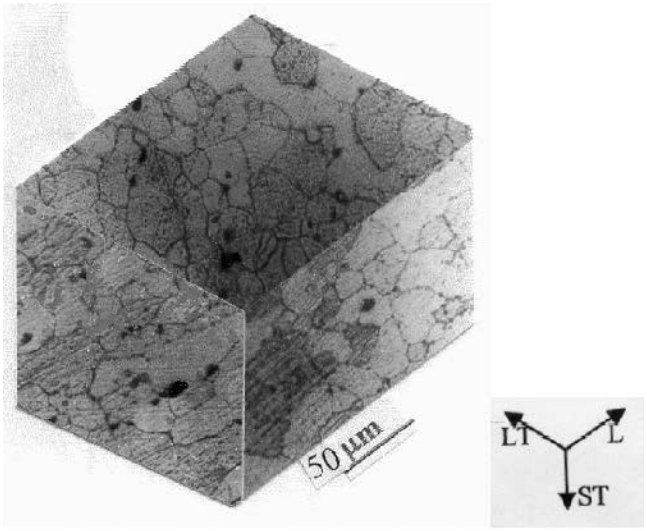

Fig. 1—Triplanar optical micrographs of the as-received peak-aged 1441 alloy.

B. *The RRA Treatment*

For hardness, TEM, DSC, XRD, and electrochemical polarization studies, coupons of approximate dimensions of 10 × 10 × 2.0 mm were cut out from the as-received alloy sheet. For tensile testing, specimens of approximate dimensions of 20-mm gage length, 4-mm width, and 1.8-mm thickness (transverse to the rolling direction) were prepared from a sheet of the alloy. The specimen thickness for all the studies was reduced to from 2.0 to 1.8 mm for removing the lithium- and magnesium-depleted zones and subsurface porosity zones developed during solutionizing of the alloy, which had been carried out at a temperature of 530 °C to 535 °C in air.[28] The surfaces were lubricated with kerosene oil, polished by emery papers of up to 600 grit, and, finally, deoiled by acetone rinsing. Retrogression treatments were applied to all the specimens of the as-received T8 temper in a vertical tube furnace in air. The retrogression temperatures selected were above and below the matrix-strengthening δ' precipitate solvus line of the Al-Li system.[29] The specimens were retrogressed for a precise time in the furnace and quenched in ice-cold water, followed by isothermal and duplex reaging to various tempers. The retrogression schedule applied to the specimens is given in Table II.

C. *Testing and Characterization Techniques*

The hardness values were measured using a Vickers hardness tester. Tensile testing was carried out using a Shimadzu Autograph universal testing machine at a crosshead speed of 2 mm/min. For TEM studies, the samples were mechanically thinned to a thickness of approximately 100 μm, punched into 3 mm discs, and, finally, thinned down to perforation using a Fischione twin-jet electropolisher, operating at 25 V and a 2.5 A current, in an electrolyte of composition 30 pct HNO_3 and 70 pct CH_3COOH at a temperature of approximately −20 °C. A PHILIPS* CM12 transmission electron microscope was used for observation of microstructures. The XRD study was carried out using a PHILIPS PW 1710 diffractometer unit with a cobalt target. The DSC runs were initiated from room temperature to around 540 °C at a heating rate of 10 °C/min in an argon atmosphere, using a Stanton Redcroft Model STA 625 (heat-flux type) simultaneous thermal analyzer. The output (the neat heat flow) relative to the reference material (high-purity annealed aluminum) was recorded as a function of temperature. A potentiodynamic polarization study was carried out in a 3.5 pct NaCl solution using a computer-controlled MEINSBERGER potentiostat/galvanostat with built-in PS6 software for assessing the effect of the RRA treatment on the electrochemical behavior of the alloy.

*PHILIPS is a trademark of Philips Electronic Instruments Corp., Mahwah, NJ.

III. RESULTS AND DISCUSSION

A. *The TEM Microstructures*

1. *The δ' (Al_3Li) Precipitation*

Figures 2(a) through (c) reveal dark-field images of the matrix-strengthening δ' precipitates of the 1441-T8, retrogressed and isothermally reaged (1441R270IA), and retrogressed and duplex-reaged (1441R230DA) tempers. The TEM studies of the retrogressed state of the alloy did not reveal any δ' phase, indicating that δ' particles had been dissolved upon retrogression treatment. Figure 2(d), the bright-field image, shows δ' precipitates in the retrogressed and duplex-reaged (1441R270DA) temper.

Figures 3(a) through (c) give a representation of the size of the δ' particles and their distribution as histograms for the T8, 1441R270IA, and 1441R230DA tempers. The size and distribution of δ' particles were analyzed using the LEICA QWIN software. The software has options for determining the area fraction and particle size of the precipitates. The volume fraction of δ' precipitates can be calculated using the expression given by Underwood[30] for spherical particles of a diameter of D:

$$f_{\delta'} = -2\ln(1-A)/D(D + 3t)$$

where A is the area fraction of the δ' particles as measured from the dark-field TEM image, and t is the thickness of the foil. In the present calculation, the mean and median of the particles have been used. For the volume-fraction calculation, the foil thickness has been taken to be of the order of 100 to 120 nm, which is, generally, the approximate TEM specimen thickness around the perforation. The calculated volume fractions of δ' precipitates for different tempers are given in Table III. The table indicates that the volume fraction of the δ' precipitates in the T8 and RRA tempers remains more or less the same. Hence, this could confirm that the strength levels of the RRA tempers would be of the same order as that of the T8 temper.

Table II. Retrogression and Reaging Schedule Applied to the As-Received, Peak-Aged 1441 Al-Li-Cu-Mg-Zr Alloy

Samples for Studies	Retrogression Temperature and Time	Reaging Schedule	RRA Temper Designation
Hardness	at 230 °C and 270 °C for 1 to 40 min	isothermal reaging at 170 °C for 2, 26, and 96 h, corresponding to the under-, peak- and overaged tempers, respectively	—
Tensile testing, XRD, TEM, DSC, and electrochemical	at 230 °C for 15 min	isothermal reaging at 170 °C for 26 h, duplex reaging at 150 °C for 36 h, followed by heating to 190 °C at a rate of 5 °C/min to 7 °C/min and holding for 1 h at the temperature	1441R230IA 1441R230DA
Polarization	at 270 °C for 5 min	isothermal reaging at 170 °C for 26 h, duplex reaging at 150 °C for 36 h, followed by heating to 190 °C at a rate of 5 °C/min to 7 °C/min and holding for 1 h at that temperature	1441R270IA 1441R270DA

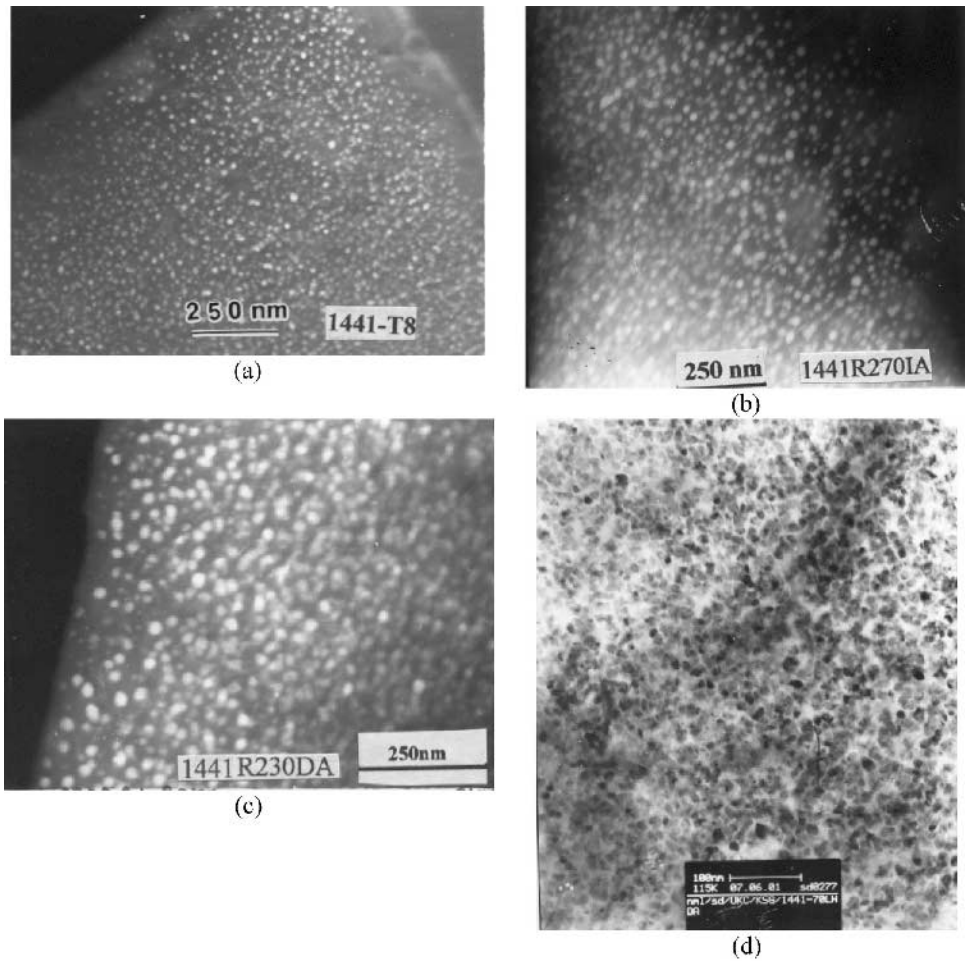

Fig. 2—Dark-field image of the matrix-strengthening δ' precipitates of (*a*) the 1441-T8, temper, (*b*) the retrogressed and isothermally reaged (1441R270IA) temper, and (*c*) the retrogressed and duplex-reaged (1441R230DA) temper. (*d*) Bright-field image of δ' precipitation in the retrogressed and duplex-reaged (1441R270DA) temper.

Figures 4(a) through (c), the representative TEM photomicrographs of the alloy in the T8 and RRA tempers, exhibits the precipitates such as β' (Al_3Zr), δ' (Al_3Li), δ (AlLi), S′ (Al_2CuMg), and T_1 (Al_2CuLi) that would be present in the alloy system. The salient features of the phases and the influence of the RRA treatment upon them are explained subsequently in brief.

2. *The β′ (Al_3Zr) Dispersoids*

Figure 4(a) shows coherent β' precipitates that are very stable, owing to the low solid solubility of Zr in Al, small misfit, and sluggish zirconium diffusion.[31,32] Because of the high stability of β' particles, the size and distribution of the particles will not be altered upon retrogression and RRA treatments. However, the dispersion of these particles

(size ranging from 20 to 30 nm in diameter) in the alloy system has multiple roles, such as inhibiting recrystallization,[33] acting as active sites for heterogeneous nucleation of matrix-strengthening δ' (Al_3Li) phase, *etc*.[34,35,36]

3. *T_1 and S′ Precipitation*

Figures 4(b) and (c), TEM bright-field images of the T8 and 1441R230DA tempers, respectively, exhibit a uniform distribution of heterogeneous precipitation of T_1 and S′ phases within the matrix. Figure 4(b) also shows the preferential heterogeneous precipitation of T_1 and S′ phases on the dislocations and equilibrium δ phase along the grain boundaries. The mechanisms of nucleation and growth of these precipitates need not be discussed, as they are similar to those of the precipitates in the Al-Li-Cu, Al-Cu-Mg, and Al-Li-Cu-Mg alloy systems, which have been discussed by many in the literature.[1,8–10] The effect of RRA treatment on the T_1 and S′ precipitates could not be assessed from the TEM photomicrographs, as the T_1 and S′ phases coprecipitate in the Al-Li-Cu-Mg-Zr alloy system. But, XRD studies (Figure 5) have revealed the effect of retrogression and RRA treatments on the precipitation of T_1 phase. The level of coprecipitation of the T_1 and S′ phases and their relative amounts depend on the alloy composition and thermal history of the alloy. The precipitation sequence and the relative proportions of the S′ and T_1 phases are critically dependent on the concentrations of all three Li, Cu, and Mg solutes. High Cu and Li contents relative to Mg result in the dominance of T_1 phase, whereas high Cu and Mg contents relative to Li cause the dominance of S′ phase.[6] The TEM studies on the microstructural changes associated with the δ', δ, T_1, S′, and β' phases, dislocation densities, the generation of more dislocation loops and helices, *etc*. for an RRA treatment applied to an 8090 Al-Li-Cu-Mg-Zr alloy have been discussed by Ghosh *et al*.[37]

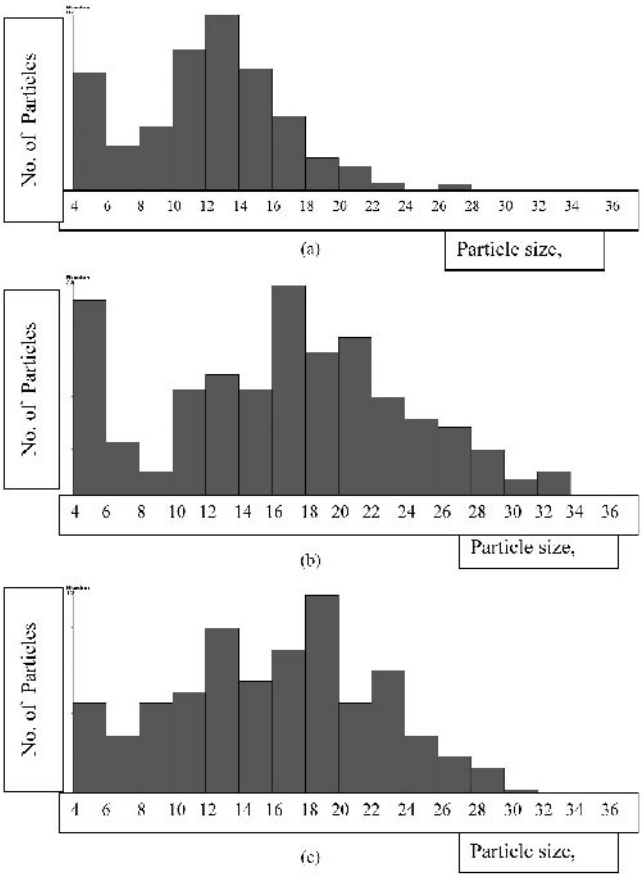

Fig. 3—Histogram of the δ' particle sizes and distributions in a representative image field of the (*a*) 1441-T8, (*b*) 1441R270IA, and (*c*) 1441R230DA tempers.

B. *The XRD Studies*

Figure 5 shows diffractograms of the alloy of various tempers (T8, retrogressed at the temperature of 270 °C for 1 and 5 minutes, retrogressed and underaged (RUA), retrogressed and isothermally aged (1441R270IA), retrogressed and duplex-aged (1441R270DA), and T7) using Co K_α radiation. The diffractograms of all the tempers show peaks of all the probable phases such the as α-Al matrix, δ' (Al_3Li), δ (AlLi), S′ (Al_2CuMg), T_1 (Al_2CuLi), and β' (Al_3Zr) precipitates that would be present in the alloy system. The diffractogram of the sample retrogressed at 270 °C for 1 minute still shows a $\delta'_{(100)}$ peak and the appearance of $T_{1(102)}$ peaks, but the diffractogram of the sample retrogressed for 5 minutes does not exhibit a $\delta'_{(100)}$ peak. The disappearance of the $\delta'_{(100)}$

Table III. Details of the δ'-Particle Image Analysis and the Estimated Volume Fraction of the δ' Precipitates

		Field 1: δ' Particle Image			Field 2: δ' Particle Image		
Alloy Temper	Foil Thickness (t), nm	Area Fraction (A)	Size (D) nm	Volume Fraction ($\times 10^{-3}$)	Area Fraction (A)	Size (D) nm	Volume Fraction ($\times 10^{-3}$)
1441–T8 (as-received)	100 to 120	0.27	mean 13.95	27.97 to 23.48	0.25	mean 12.57	23.14 to 19.42
			median 14.50	29.02 to 24.37		median 13.00	23.60 to 20.05
1441R270IA	100 to 120	0.26	mean 16.86	32.04 to 26.94	0.19	mean 17.19	22.84 to 19.20
			median 17.00	32.30 to 27.16		median 19.00	25.10 to 21.13
1441R230DA	100 to 120	0.24	mean 16.18	28.04 to 23.60	0.22	mean 15.25	24.04 to 20.20
			median 17.00	26.14 to 24.75		median 15.00	23.67 to 19.88

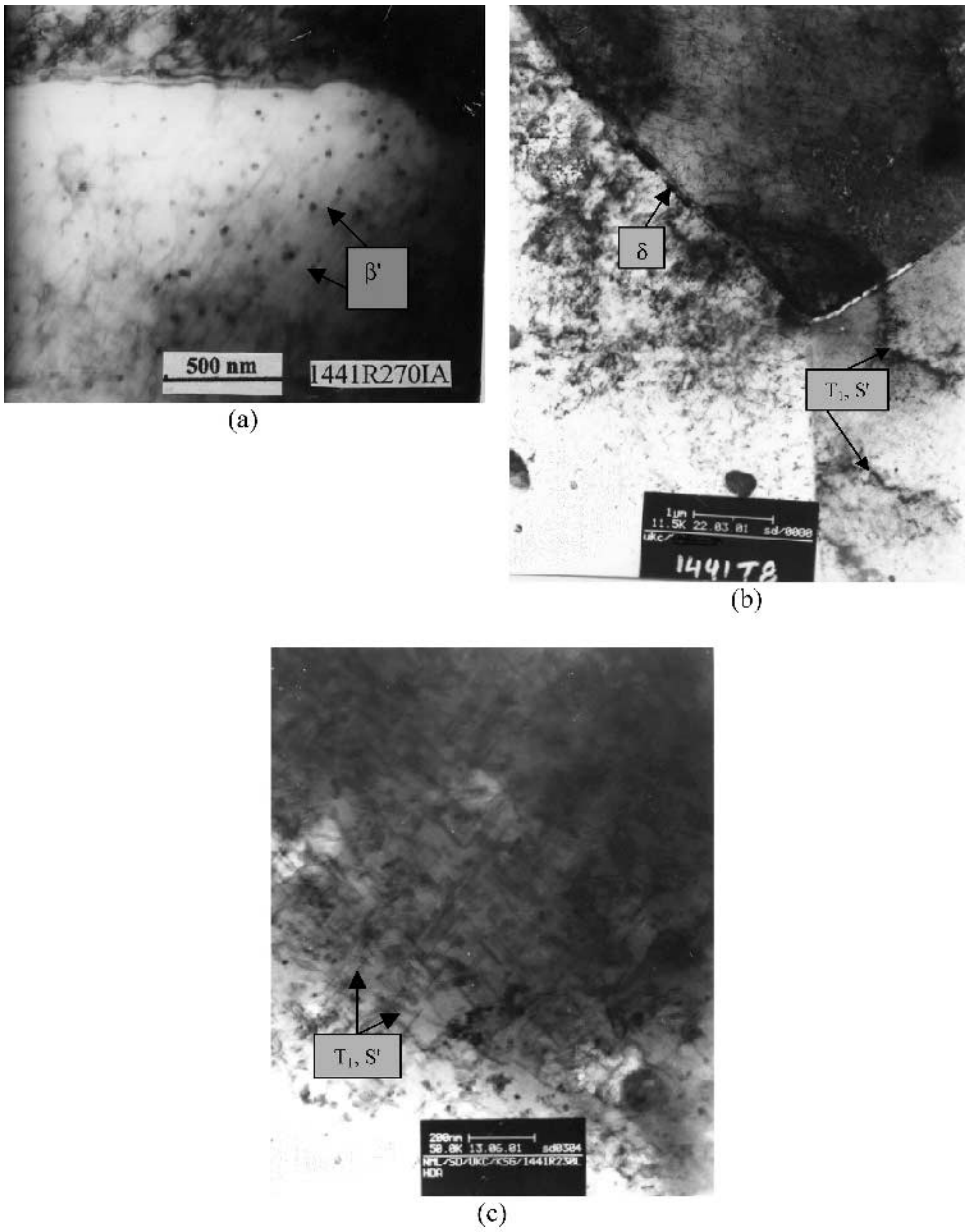

Fig. 4—Representative TEM photomicrographs of (*a*) the 1441R270IA RRA temper, exhibiting β' (Al_3Zr) dispersoids; (*b*) the 1441-T8 temper, showing β' dispersoids within the grains, uniform homogeneous and heterogeneous (preferentially along the dislocations) precipitation of S′ (Al_2CuMg) and T_1 (Al_2CuLi) phases, and equilibrium δ (AlLi) phase along the grain boundaries; and (*c*) the 1441R230DA temper, revealing a uniform distribution of S′ and T_1 phases.

peak is attributed to the dissolution of δ' phase in the solid solution. The diffractogram of the sample retrogressed at 270 °C for 1 minute indicates that dissolution of δ' phase has commenced with retrogression, but has partially dissolved into solid solution, and the remaining δ' phase in the matrix could still be detected by XRD. The diffractogram of the sample retrogressed at 270 °C for 5 minutes indicates that the time of 5 minutes has caused enough dissolution of δ' phase into solution. The appearance of an additional $T_{1(102)}$ peak and other intensified peaks of the T_1 and δ phases is due to fact that as δ' phase dissolves into solid solution during retrogression, the lithium content of the solid solution increases, which causes δ, T_1, and S′ phases to nucleate and grow. The diffractograms of the RRA tempers show the reappearance of the $\delta'_{(100)}$ peak with the presence of the other additional peaks of T_1 and δ phases that have formed during retrogression. The effect of the RRA treatment on the S′ phase could not be explained from the XRD studies, as the peaks of $Al_{(111)}$, $Al_{(200)}$, $\beta'_{(114)}$, and $\beta'_{(200)}$ overlap with the S′-phase peaks.

C. *The DSC Studies*

The DSC studies provide complimentary information on phase transformation in addition to that obtained by means of other metallurgical techniques. In particular, precipitated particles or zones can be detected by their dissolution peaks during temperature scanning, even if their sizes are not large enough for an easy TEM characterization.

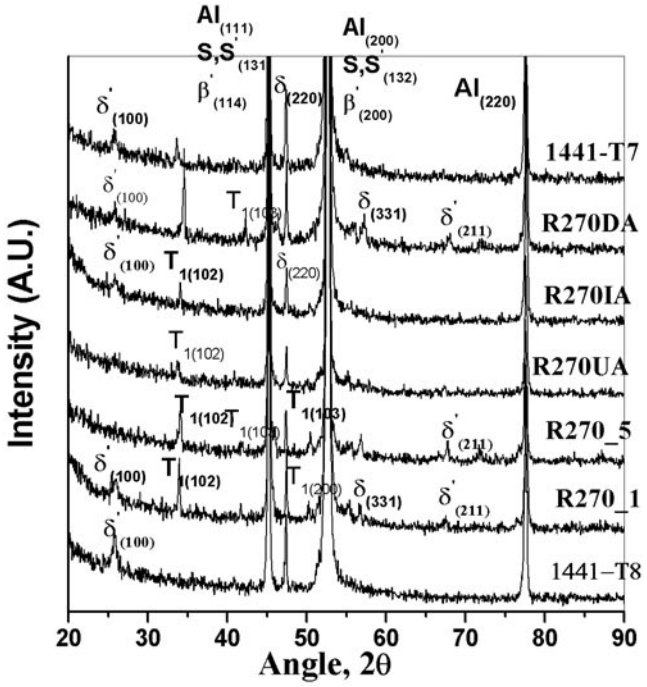

Fig. 5—XRD of the 1441 alloy of various tempers using Co K_α radiation. The notation "R270_1" indicates retrogression at 270 °C for 1 min.

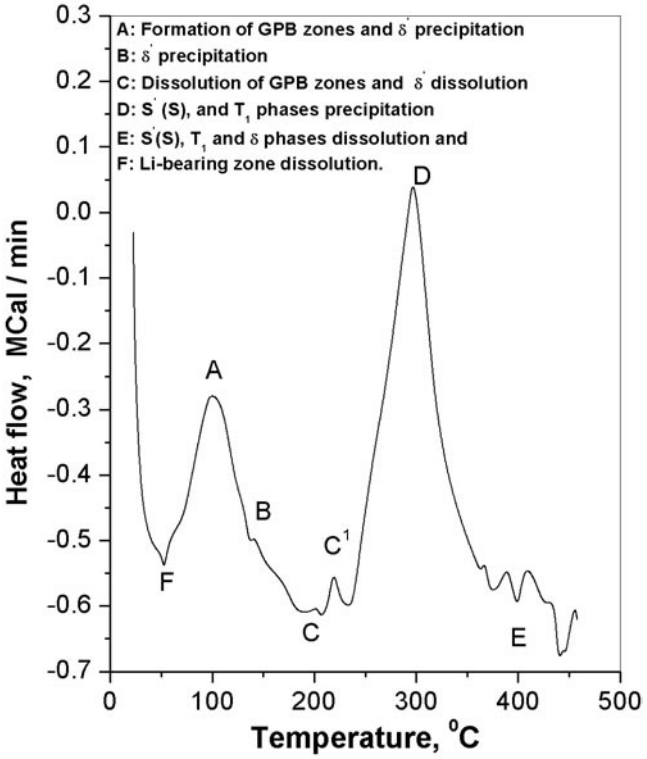

Fig. 6—DSC thermogram of the solution-treated and water-quenched 1441 alloy at a heating rate of 10 °C/min.

Figure 6 shows a DSC thermogram of a solution-treated and water-quenched 1441 alloy at a heating rate of 10 °C/min. Figures 7(a) through (c) show DSC thermograms of the alloy in the T8, retrogressed at 230 °C (1441R230), and RRA (1441R230DA) tempers.

The thermogram (Figure 6) exhibits many exothermic and endothermic peaks (marked with the letters A through F), indicating the sequence of precipitation and dissolution reactions. The precipitation reactions are as follows. A: the formation of Guinier-Preston-Bagaratsky GPB zones and precipitation of the δ' phase; C: the dissolution of GPB zones and δ' precipitates; D: the precipitation of S′ (S), T_1, and δ phases; E: the dissolution of S′ (S), T_1, and δ phases; and F: the dissolution of Li-bearing zone. The peaks of the precipitation/dissolution reactions and the corresponding temperature range are in close agreement with those mentioned in literature.[38,39,40] The peak region B is the temperature zone for the precipitation of δ' phase in the Al-Li-Cu-Mg-Zr alloy system, as reported in the literature.[38,39,40] However, the precipitation of δ' phase in the peak region B for the 1441 alloy is not clearly resolved with a sharp peak; instead, a small thermal fluctuation is observed. The presence of Cu and Mg decreases the Li solubility in Al alloys, which favors both the precipitation and growth of δ' particles, mostly in the first stages of aging, *i.e.*, at the lower-temperature range, and the δ' solvus line of this 1441 alloy is also in the lower range.[29] Thus, these factors cause precipitation of δ' phase at a lower temperature, resulting in overlapping of the peak B region of δ' precipitation with the peak A region of GPB zone formation. Due to the overlapping of the GPB-zones formation and δ' precipitation, it is not easy to determine kinetic parameters of the phases by varying the heating-rate method. Further, the overlapping of the peak regions A and B does not confirm the presence of δ' precipitates in the alloy from the DSC study. However, DSC thermogram of the retrogressed state showed that these two peaks have appeared at separate temperatures, which is discussed in the next paragraph.

Figure 7(a), the thermogram of the T8 temper, exhibits two clear endothermic-peak regions (C and E) and an exothermic-peak region (D). In the peak region D, two distinct peaks (D_1 and D_2) are seen. The clearly revealed D_1 and D_2 peaks indicate that the precipitations of S′, S, T_1, T_2, and δ phases have taken place at different temperatures as compared to that of the solution-treated and water-quenched condition (Figure 6). The absence of lower-temperature exotherms, *i.e.*, peak A and B in the T8 and RRA tempers (Figures 7(a) and (c)), indicates that the alloy is not supersaturated with the solute elements Li, Cu, and Mg, as these tempers had equilibrium amounts of δ' precipitates in the matrix. But, Figure 7(b), the thermogram of the retrogressed (1441R230) state, exhibits the lower-temperature exotherms, *i.e.*, peaks A and B, separately. In the retrogressed state, the solid solution is supersaturated with Li atoms because of the dissolution of δ' (Al_3Li) phase into solution during the retrogression treatment. Therefore, the reappearance of the peak regions A and B in the DSC thermogram is quite obvious. Further, the retrogressed state, being supersaturated only with Li atoms in the solid solution, requires higher thermal energy for δ'-phase precipitation compared to that required in the solution-treated, water-quenched state, which is supersaturated with all of the solutes (Cu, Li, and Mg). Hence, the precipitation of δ' in the retrogressed temper would occur at higher temperatures than that in the water-quenched state. Therefore, the peaks A (the formation of GPB zones) and B (the precipitation of δ' phase) have appeared separately for the retrogressed state (Figure 7(b)) and would enable to

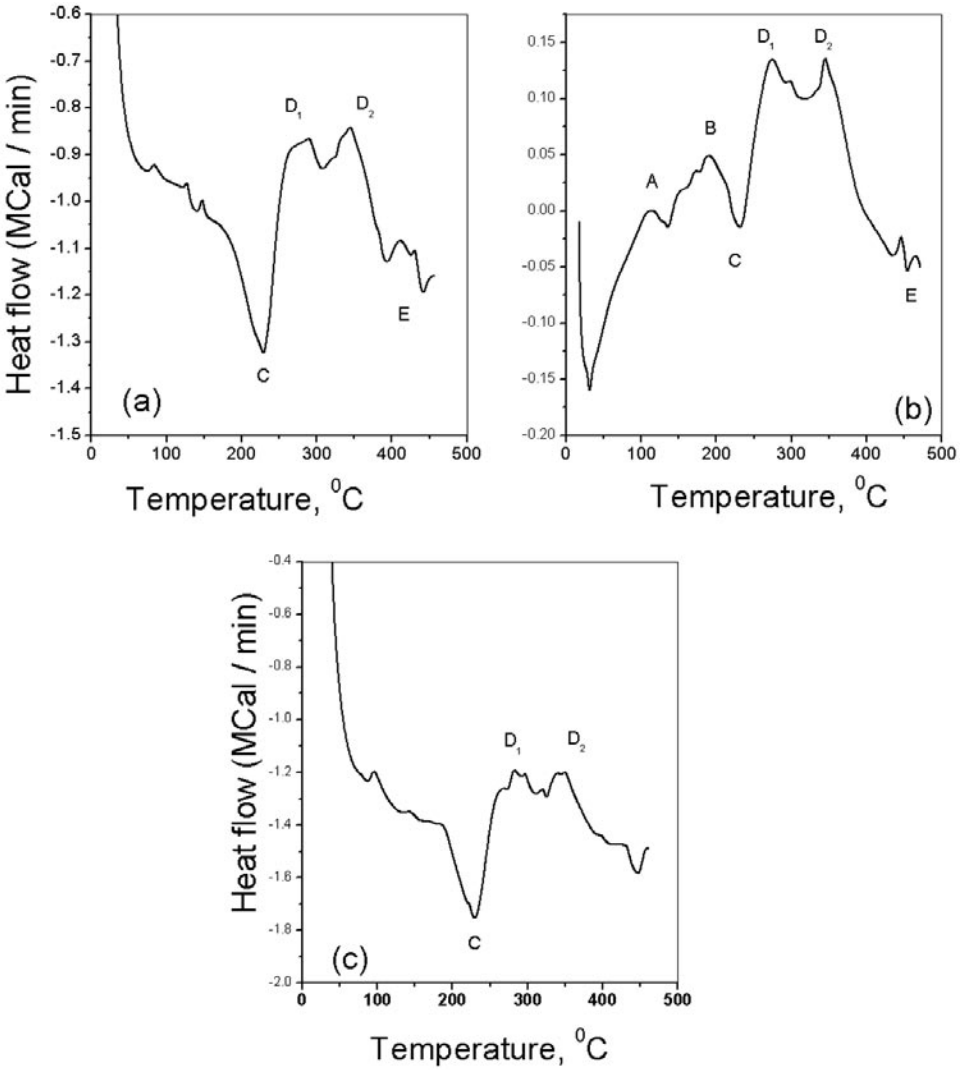

Fig. 7—DSC thermograms of the (*a*) 1441-T8, (*b*) 1441R230, and (*c*) 1441R230DA tempers at a heating rate of 10 °C/min.

determine of kinetic parameters by the varying heating-rate method. Figure 7(c), the DSC thermogram of the 1441R230DA temper, shows the peak regions C, D, and E, similar to that of the observation in the T8 temper.

D. *Hardness Measurement and Tensile Properties*

Figure 8 exhibits the variation of hardness with retrogression time at the retrogression temperatures of 215 °C, 230 °C, and 270 °C. The graphs display the characteristic behavior of retrogression phenomenon, *i.e.*, an initial sharp decrease in hardness with retrogression time and the attainment of a minimum followed by a slight increase, after which there is no further change in hardness with retrogression time. Similar trends of the results are also reported in the literature for 7*xxx* and 8*xxx* alloy series.[17–20] Further, the curves show that the greater the retrogression temperature, the greater is the drop of hardness and the less is the retrogression time for attaining the minimum hardness.

Figure 9 exhibits the variation of hardness with retrogression time at the retrogression temperature of 270 °C and the change in hardness on subsequent reaging to the under-, peak-, and over-aged tempers. The figures indicate that reaging the retrogressed temper has led to regaining of hardness.

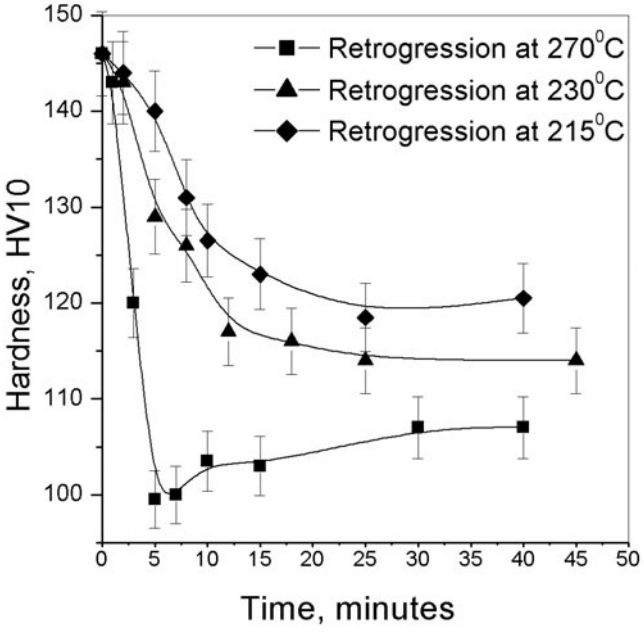

Fig. 8—Variation of hardness with retrogression time at different retrogression temperatures of the 1441 alloy.

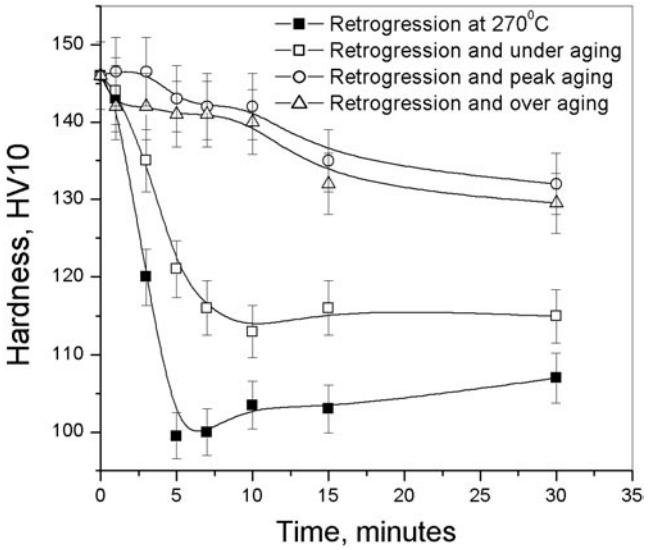

Fig. 9—Variation of hardness with retrogression time and reaging to various tempers of the 1441 alloy.

But, for longer retrogression times (*i.e.*, the time beyond the minimum hardness), reaging even to the peak-aged temper failed to achieve the initial T8 hardness value. This is due to the fact that the longer retrogression time at the retrogression temperature (which is higher than the artificial peak-aging temperature) leads to the overaged T7 temper.

Table IV gives the average values of the yield strength, ultimate tensile strength, and plastic strain to fracture for various tempers of the alloy. Tests are repeated to confirm the results, and the values are in conformity with those for the corresponding tempers reported in the literature.[17,41] The retrogression tempers have lower yield- and ultimate-strength values compared to the T8 and RRA tempers. The higher the retrogression temperature, the greater is the decrease in strength. The strength value of the RUA temper is higher than the values of the retrogressed tempers, but lower than those of the T8 and RRA tempers. The strength properties of the RRA tempers are in close proximity to those of the T8 temper. It is to be noticed that although the total aging time of the RRA tempers is almost twice that of the conventional T8 temper, the RRA tempers have strength properties in the same range as in the T8 temper.

The initial decrease of hardness with retrogression time is attributed to the preferential dissolution of the matrix-strengthening δ' precipitates, which are no longer stable at the retrogression temperature, as observed in TEM, XRD (Figure 5), and DSC (Figure 7(b)) studies. The decrease of hardness and strength values upon retrogression could also be due to the decrease of the dislocation density.[16,17] But, during retrogression, other precipitates like β', T_1, and S′ (S) remain mostly undissolved;[42] however, the growth of the Li-bearing phases, particularly T_1 and δ, can occur. The minimum in the retrogression curve is indicative of the maximum dissolution of δ' precipitates. The retrogression time beyond the corresponding minimum hardness can cause slight hardening owing to the onset of a structural age-hardening effect, and this is in conformity with available literature,[15,17] which states that initially, the dissolution rate is greater than the precipitation rate, but, beyond a critical point, the precipitation rate exceeds the dissolution rate. The greater decrease of hardness and strength values at higher retrogression temperatures (Figure 8 and Table IV) is due more to dissolution of δ' precipitates and less to dislocation densities.[16,17,25,37] Further, the faster drop in hardness with retrogression temperature (Figure 8), requiring less retrogression time to minimum hardness, is consistent with the concept of faster dissolution kinetics with increasing temperature.

Table IV. Average Values of Tensile Properties of the 1441 Alloy of Various Tempers Tested at a Crosshead Speed of 2 mm/min in Air

Alloy Temper	Yield Strength, MPa	Ultimate Tensile Strength, MPa	Plastic Strain to Fracture (ε_p), Pct
1441-T8	395	447	8.00
1441R230	330	387	11.50
1441R270	325	374	12.39
1441R230UA (170_2)	350	404	9.15
1441R270UA (170_2)	355	412	9.65
1441R230IA	390	443	7.75
1441R270IA	380	440	7.80
1441R230DA	400	449	8.05
1441R270DA	390	442	8.15
1441-T7	380	430	7.50

Reaging the retrogressed states causes the reprecipitation of δ' precipitates in the matrix, which results in bringing back the hardness and strength values. Reaging the retrogressed state to the peak-aged (RRA) temper causes complete reprecipitation of the matrix-strengthening δ' precipitates and, hence, the strength properties of the RRA tempers are at the same level as those of the T8 temper. Reaging the retrogressed state to the underaged (RUA) temper causes only partial reprecipitation of δ' phase. So, the hardness and strength of the RUA tempers are higher than those of the retrogressed tempers but are lower than that of the RRA tempers (Figure 9 and Table IV).

E. *The SEM Fractography*

Figures 10(a) through (c) show representative SEM fractographs of the tensile samples of the T8, retrogressed (1441R270), and T7 tempers of the alloy. The fractographs reveal cracking mostly along grain boundaries, or intergranular failure, and subintergranular failure along the subgrain boundaries and extremely small areas with dimples. The fractographs have more or less the same features irrespective of the aging tempers studied. Fractographs of the retrogressed temper exhibit more dimples compared to those in the T8 and T7 tempers.

In the T8, RRA, and T7 tempers, the presence of coherent shearable δ' precipitates leads to inhomogeneous slip, causing severe strain localization during deformation.[43] This strain localization arises because of the interaction of mobile dislocations with the ordered coherent and partially coherent particles dispersed in the matrix. The strain localization due to concentrated deformation in planar-slip bands and at the point of their impingement on grain boundaries is one of the reasons for crack initiation. The mechanism of intergranular cracking

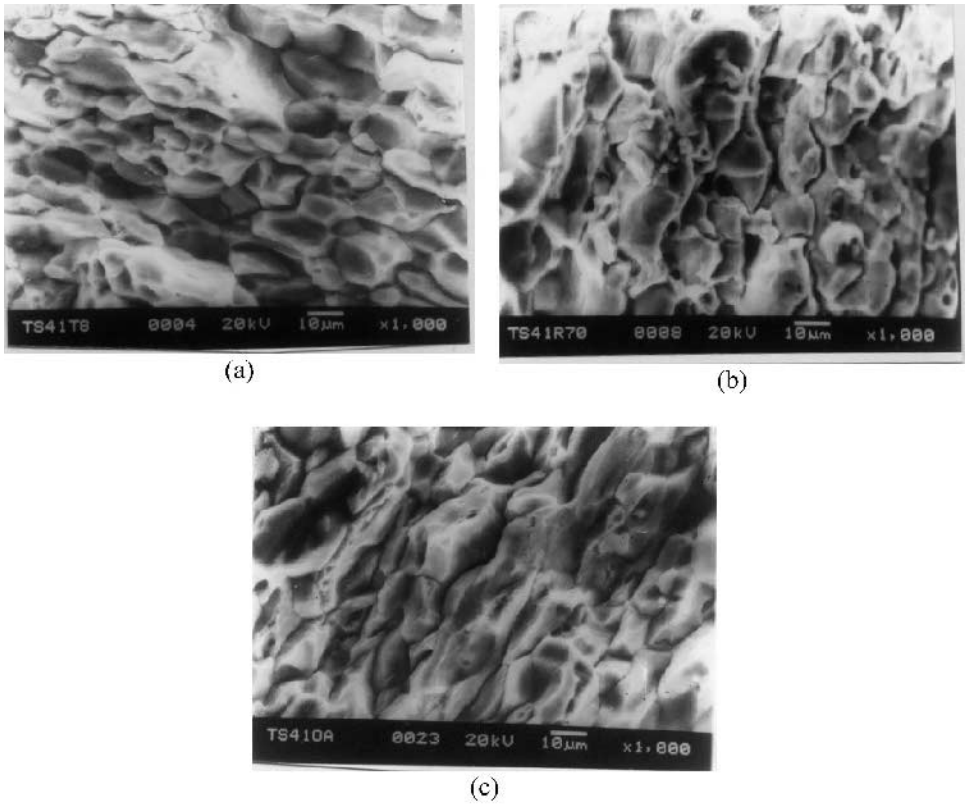

Fig. 10—Representative SEM fractographs of the tensile samples of (*a*) the as-received, peak-aged 1441-T8 temper, (*b*) the retrogression at the temperature of 270 °C for 5 min (*i.e.*, the 1441R270 temper), and (*c*) the over-aged 1441-T7 temper, showing intergranular and subintergranular cracks and grain-boundary voids and extremely small areas of dimples.

in the 8090 Al-Li-Cu-Mg-Zr alloy has been discussed by Srivatsan[44] and Lavernia *et al.*[45] in detail. Void initiation occurs at the intersection of a slip band and at the coarse grain-boundary precipitates. The applied stress assists in the growth of voids. Linking of voids is an additional factor that promotes or enhances intergranular fracture.

The fractograph of the retrogression temper (Figure 10(b)) also shows intergranular and subintergranular cracking and extremely small areas of dimples. The retrogressed state contains a low dislocation density[25] as well as a low volume fraction of δ' precipitates. Thus, the strain localization arising due to the interaction of mobile dislocations with δ' precipitates is less operative, accounting for the higher ductility in the retrogressed temper (Table IV). But, the strain localization due to the presence of the grain-boundary equilibrium δ precipitates remains operative, and, hence, the initiation of microvoids near the grain boundaries leads to intergranular cracking. Areas with fine dimples are also seen within the separated grains. The formation of such microdimples has been explained in detail by Srivatsan.[44]

F. *Electrochemical Behavior*

Figure 11 shows potentiodynamic polarization curves in 3.5 pct NaCl solution of the alloy in the T8, RRA, and T7 tempers. The shape of the polarization curves is similar for all the tempers of the alloy in the environment studied. The curves show that the open-circuit potential (OCP) values have shifted to more negative potentials with aging time. Similar trends are also reported in the literature.[46,47] The OCP of the T7 temper has the most negative value, whereas the OCP values of the RRA tempers lie in between the OCP values of the T7 and T8 tempers.

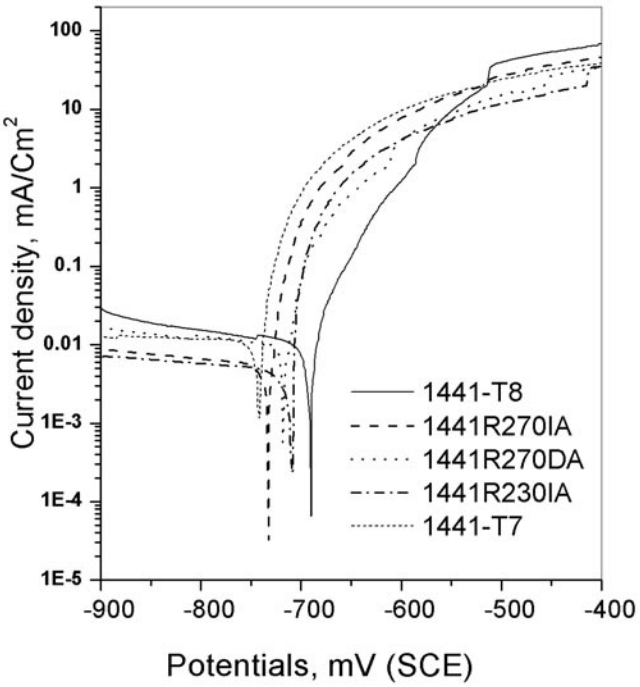

Fig. 11—Potentiodynamic polarization curves of the 1441 alloy of various tempers in 3.5 pct NaCl solution at a scan rate of 0.5 mV/s.

The OCP of an alloy in a given environment depends on the alloy composition, solute content in the solid solution, and nature and relative amounts of the constituent phases. Thus, the shifting of the OCP toward a more-negative direction (anodic) for the RRA tempers compared to that of the conventional T8 tempers can be attributed to the presence of higher amounts of δ, T_1, and S' phases[37,48–50] (Figures 4 and 5), which are anodic in nature. It is an established fact that the microstructures of the T7 temper in precipitation-hardening aluminum alloys contain higher amounts of equilibrium phases. Thus, in the RRA and T7 tempers of this 1441 alloy also, the microstructure comprises higher amounts of equilibrium δ phase, as the transformation takes place from δ' (Al_3Li) to equilibrium δ (AlLi) upon RRA treatment and with the progress of the aging process for longer aging time. Therefore, based on the shifting of OCP values toward the more-negative (anodic) direction of the RRA tempers compared to the as-received T8 temper, it can be inferred that the microstructure of the RRA tempers approaches that of the T7 temper.

IV. CONCLUSIONS

1. The TEM, XRD, and DSC studies of the as-received 1441 alloy revealed the presence of all the phases, such as the α-Al matrix, δ' (Al_3Li), δ (AlLi), S' (Al_2CuMg), T_1 (Al_2CuLi), and β' (Al_3Zr), that are likely to be present in the alloy system. Retrogression causes dissolution of the matrix-strengthening δ' phase in the solid solution, and reaging the retrogressed state causes reprecipitation of δ' phase in the matrix. Further, XRD studies exhibited an additional peak or intense peaks of T_1 and δ phases in the retrogressed and RRA tempers.
2. The overlapping peaks of GPB-zone formation and δ' precipitation in the thermogram of the solution-treated, water-quenched state will not enable a determination of the kinetic parameters such as activation energy by varying the heating-rate method. However, the separate appearance of peaks for GPB-zone formation and δ' precipitation in the thermogram of the retrogressed state would enable one to overcome the difficulty.
3. Retrogression treatment results in a decrease in the hardness and tensile strength and an increase in the ductility, which is attributed to the dissolution of δ' phase into the solid solution. Reaging the retrogressed state results in restoration of the mechanical properties, as reaging causes reprecipitation of δ' phase in the matrix. Reaging the retrogressed state to the peak-aged (RRA) temper caused restoration of the initial T8 strength properties.
4. The OCP values of the RRA tempers lie in between that of the T8 and T7 tempers. The shifting of the OCP values toward anodic direction in the RRA and T7 tempers, is attributed to the precipitation of a higher amount of anodic phases such as δ and T_1 and S'. Thus, the microstructure of the RRA tends to that of the T7 temper while maintaining the conventional T8 temper strength properties.

ACKNOWLEDGMENTS

The authors thank Mr. Samar Das, National Metallurgical Laboratory (Jamshedpur, India), for TEM studies, and Mr. Nirmal Das, Central Research Facility, Indian Institute of Technology (Kharagpur, India), for carrying out DSC studies.

REFERENCES

1. *Aluminum and Aluminum Alloys*, ASM Specialty Handbook, J.R. Davis, ed., ASM INTERNATIONAL, TMS, Materials Park, OH, 1998, pp. 121-42.
2. E.J. Lavernia, T.S. Srivatsan, and F.A. Mohamed: *J. Mater. Sci*., 1990, vol. 25, pp. 1137-58.
3. K.K. Sankaran and N.J Grant: *Aluminum Lithium I*, Proc 1st Int. Conf. Aluminum Lithium Alloys, T.H. Sanders, Jr. and E.A. Starke, Jr., eds., TMS, Warrendale, PA, 1981, pp. 205-27.
4. P.J. Gregson and H.M. Flower: *Proc. Int. Conf. on Aluminum Technology '86*, T. Sheppard, ed., The Institute of Metals, London, 1986, pp. 423-28.
5. P.J. Gregson, H.M. Flower, C.N.J. Tite, and A.K. Mukhopadhyay: *Mater. Sci. Technol*., 1986, vol. 2, pp. 349-53.
6. W.S. Miller, J. White, and D.J. Lloyd: *Aluminum Lithium Alloys IV*, Proc. 4th Int. Conf. on Aluminum Lithium Alloys, G. Champier, B. Dubost, D. Miannay, and L. Sabetay, eds.; *J. Phys*., 1987, vol. 48, Suppl., pp. C3:131-C3:149.
7. R.C. Dorward and K.R. Hasse: *Corr.—NACE*, 1987, vol. 43, pp. 408-23.
8. N.J.H. Holroyd, A. Gray, G.M. Scamans, and R. Hermann: *Aluminum Lithium Alloys III*, Proc. 3rd Int. Conf. on Aluminum Lithium Alloys, C. Baker, P.J. Gregson, S.J. Harris and C.J. Peel, eds., The Institute of Metals, London, 1986, pp. 310-20.
9. F. Binsfeld, M. Habashi, J. Galland, J.P. Fidelle, D. Minnay, and P. Rofidal: *Aluminum Lithium Alloys IV*, Proc. 4th Int. Conf. on Aluminum Lithium Alloys, G. Champier, B. Dubost, D. Miannay, and L. Sabetay, eds., *J. Phys*., 1987, vol. 48, Suppl., pp. C3:587-C3:596.
10. B. Cina: United States Patent No. 3,856,584, Dec. 24, 1974.
11. B. Cina and B. Ranish: Paper No. XXV, Aluminum Industrial Products, ASM, Pittsburgh, PA, 1974.
12. K. Ural: *J. Mater. Sci. Lett*., 1984, vol. 13, pp. 383-85.
13. N.C. Danh, K. Rajan, and W. Wallace: *Metall. Trans. A*, 1983, vol. 14A, pp. 1843-50.
14. M. Kanno, I. Araki, and Q. Cui: *Mater. Sci. Technol*., 1994, vol. 10, pp. 599-603.
15. K. Rajan, W. Wallace, and J.C. Beddoes: *J. Mater. Sci*., 1982, vol. 17, pp. 2817-24.
16. M. Talianker and B. Cina: *Metall. Trans. A*, 1989, vol. 20A, pp. 2087-92.
17. C. Thakur and R. Balasubramaniam: *Acta Mater*., 1997, vol. 45, pp. 1323-32.
18. J.K. Park: *Mater. Sci. Eng*., 1998, vol. A103, pp. 223-31.
19. M.B. Hall and J.W. Martin: *Z. Metallkd*, 1994, vol. 85, pp. 134-39.
20. M.U. Islam and W. Wallace: *Metals Technol*., 1983, vol. 10, pp. 386-92.
21. M.U. Islam and W. Wallace: *Metals Technol*., 1984, vol. 11, pp. 320-22.
22. M. Ahmad: *Mater. Sci. Eng*., 1990, vol. A125, pp. 1-14.
23. J.S. Robinson: *Mater. Sci. Forum*, 2000, vols. 331–337, pp. 1653-58.
24. A. Gray, N.J.H. Holroyd, and J. White: *Aluminum Lithium Alloys V*, Proc. 5th Int. Conf. on Aluminum Lithium Alloys, T.H. Sanders, Jr., and E.A. Starke, Jr., eds., Materials and Component Engineering Publications, Warrendale, PA, 1989, pp. 1175-86.
25. V. Komisarov, M. Tlianker, and B. Cina: *Mater. Sci. Eng*, 1996, vol. A221, pp. 113-21.
26. V. Komisarov, M. Tlianker, and B. Cina: *Mater. Sci. Eng*., 1989, vol. A242, pp. 39-49.
27. Z.Q. Hu, Y. Zhang, Y.L. Liu, and Z.Y. Zhu: *Corrosion*, 1993, vol. 49, pp. 491-98.
28. S. Fox, H.M. Flower, and D.C. McDarmaid: *Aluminum Lithium Alloys III*, Proc. 3rd Int. Conf. on Aluminum Lithium Alloys, C. Baker, P.J. Gregson, S.J. Harris, and C.J. Peel, eds., The Institute of Metals, London, 1986, pp. 263-72.
29. O. Jensrud and N. Ryum: *Mater. Sci. Eng*., 1984, vol. 64, pp. 229-36.
30. E.E. Underwood: in *Quantitative Stereology*, M. Cohen, ed., Addison Wesley, Reading, MA, 1970, p. 178.
31. N. Tryum: *Acta Metall*., 1969, vol. 17, p. 269.
32. H.M. Flower and P.J. Gregson: *Mater. Sci. Technol*., 1987, vol. 3, pp. 81-90.

33. N. Nes: *Acta Metall*., 1972, vol. 20, p. 499.
34. P.J. Gregson and H.M. Flower: *J. Mater. Sci. Lett*., 1984, vol. 3, pp. 829-34.
35. F.W. Gayle and J.B. Vandersande: *Scripta Metall*., 1984, vol. 18, pp. 473-78.
36. F.W. Gayle and J.B. Vandersande: *Proc. Conf. Aluminum Alloys—Their Physical and Mechanical Properties*, E.A Starke and T.H. Sanders, eds., Engineering Materials Advisory Service, Warley, 1986, vol. II, p. 727.
37. K.S. Ghosh, K. Das, and U.K. Chatterjee: *Mater. Sci. Technol*., 2004, vol. 20, pp. 825-34.
38. A. Luo, D.J. Lloyd, A. Gupta, and W.V. Youdelis: *Acta Metall. Mater*., 1993, vol. 41, pp. 769-76.
39. M.L. Starink and P.J. Gregson: *Scripta Metall*., 1995, vol. 33, pp. 893-900.
40. A.K. Mukherjee, C.N.J. Tite, H.M. Flower, P.J. Gregson, and F. Sale: *Aluminum Lithium Alloys IV*, Proc. 4th Int. Conf. on Aluminum Lithium Alloys, G. Champier, B. Dubost, D. Miannay, and L. Sabetay, eds., *J. Phys*., 1987, vol. 48, Suppl., pp. C3:439-C3:446.
41. G.M. Reddy, A.A. Gokhale, and K. Prasad Rao: *Sci. Technol. Welding Joining*, 1998, vol. 3, pp. 151-58.
42. R.E. Ricker, J.L. Fink, and A.K. Vasudevan: *Metall. Trans. A*, 1991, vol. 22A, pp. 264-67.
43. C.P. Blankenship, Jr. and E.A. Starke: *Metall. Trans. A*, 1993, vol. 22A, pp. 833-41.
44. T.S. Srivatsan and T. Allan Place: *J. Mater. Sci*., 1989, vol. 24, pp. 1543-51.
45. I.J. Lavernia, T.S. Srivatsan, and F.A. Mohamed: *J. Mater. Sci*., 1990, vol. 25, pp. 1137-58.
46. A. Gray: *Aluminum Lithium Alloys IV*, Proc. 4th Int. Conf. on Aluminum Lithium Alloys, G. Champier, B. Dubost, D. Miannay, and L. Sabetay, eds., *J. Phys*., 1987, vol. 48, Suppl., pp. C3:891-C3:904.
47. J.M. Sater and T.H. Sanders: *Aluminum Lithium Alloys V*, Proc. 5th Int. Conf. on Aluminum Lithium Alloys, T.H. Sanders, Jr. and E.A. Starke, Jr., eds., Materials and Component Engineering Publications, Warrendale, PA, 1989, pp. 1217-25.
48. M. Reboul and P Meyer: *Aluminum Lithium Alloys IV*, Proc. 4th Int. Conf. on Aluminum Lithium Alloys, G. Champier, B. Dubost, D. Miannay, and L. Sabetay, eds., *J. Phys*., 1987, vol. 48, Suppl., pp. C3:881-C3:889.
49. J. Garcia, P. Ponthiaux, M. Habashi, and J. Galland: *Aluminum Lithium Alloys IV*, Proc. 4th Int. Conf. on Aluminum Lithium Alloys, G. Champier, B. Dubost, D. Miannay, and L. Sabetay, eds., *J. Phys*., 1987, vol. 48, Suppl., pp. C3:861-C3:870.
50. B. Bavarian, J. Becker, S.N. Parikh, and M. Zamanzadeh: *Aluminum Lithium Alloys V*, Proc. 5th Int. Conf. on Aluminum Lithium Alloys, T.H. Sanders, Jr. and E.A. Starke, Jr., eds., Materials and Component Engineering Publications, Warrendale, PA, 1989, pp. 1227-36.